Atmos. Chem. Phys., 15, 6113–6125, 2015
www.atmos-chem-phys.net/15/6113/2015/
doi:10.5194/acp-15-6113-2015

Atmospheric Chemistry and Physics
Open Access

Ice crystal concentrations in wave clouds: dependencies on temperature, $D > 0.5\,\mu m$ aerosol particle concentration, and duration of cloud processing

L. Peng, J. R. Snider, and Z. Wang

Department of Atmospheric Sciences, University of Wyoming, Laramie, WY, USA

Correspondence to: J. R. Snider (jsnider@uwyo.edu)

Received: 26 July 2014 – Published in Atmos. Chem. Phys. Discuss.: 23 October 2014
Revised: 21 April 2015 – Accepted: 1 May 2015 – Published: 4 June 2015

Abstract. Model equations used to either diagnose or prognose the concentration of heterogeneously nucleated ice crystals depend on combinations of cloud temperature, aerosol properties, and elapsed time of supersaturated-vapor or supercooled-liquid conditions. The validity of these equations has been questioned. Among many uncertain factors there is a concern that practical limitations on aerosol particle time of exposure to supercooled-liquid conditions, within ice nucleus counters, has biased the predictions of a diagnostic model equation. In response to this concern, this work analyzes airborne measurements of crystals made within the downwind glaciated portions of wave clouds. A streamline model is used to connect a measurement of aerosol concentration, made upwind of a cloud, to a downwind ice crystal (IC) concentration. Four parameters are derived for 80 streamlines: (1) minimum cloud temperature along the streamline, (2) aerosol particle concentration (diameter, $D > 0.5\,\mu m$) measured within ascending air upwind of the cloud, (3) IC concentration measured in descending air downwind, and (4) the duration of water-saturated conditions along the streamline. The latter are between 38 and 507 s and the minimum temperatures are between -34 and $-14\,^{\circ}C$. Values of minimum temperature, $D > 0.5\,\mu m$ aerosol concentration, and IC concentration are fitted using the equation developed for ice nucleating particles (INPs) by by DeMott et al. (2010; D10). Overall, there is reasonable agreement among measured IC concentrations, INP concentrations derived using D10's fit equation, and IC concentrations derived by fitting the airborne measurements with the equation developed by D10.

1 Introduction

Ice nucleation is a pivotal process in the evolution of many cloud types (Braham and Squires, 1974; Cantrell and Heymsfield, 2005; DeMott et al., 2010; Murray et al., 2012). Ice crystals form via different pathways; the two fundamental distinctions are homogeneous and heterogeneous nucleation. Temperatures colder than $-35\,^{\circ}C$ and the existence of either haze particles or cloud droplets are necessary conditions for the occurrence of the homogeneous pathway (Heymsfield and Miloshevich, 1993). Heterogeneous ice nucleation takes place on ice nucleating particles (INPs) and the known pathways are deposition, condensation freezing, immersion freezing, and contact freezing (Vali, 1985; Murray et al., 2012).

Two contrasting approaches are used to translate measurements into equations used to predict INP activation, and thus ice crystal (IC) concentration, in cloud models. The first of these is diagnostic in the sense that IC concentration is formulated solely in terms of thermodynamic and aerosol state properties. The second is state and time dependent. In model intercomparison studies (Eidhammer et al., 2009; Niemand et al., 2012), these two frameworks produce significantly different IC concentrations. There are many reasons for these inconsistencies; fundamentally, they result because the timescale characterizing the development of a subcritical ice embryo into an ice crystal (Bigg, 1953; Vali and Stansbury, 1966) and how properties of an ice nucleating particle influences embryo development are inadequately understood (Murray et al., 2012; Vali, 2014). Another relevant factor, but one which attenuates the framework-to-framework differences (Eidhammer et al., 2009), is that the Bergeron–

Findeisen process can act to slow, or even shut down, the freezing nucleation pathways (i.e., condensation, immersion, and contact freezing).

Our primary focus is the temperature- and aerosol-dependent fit equation developed by DeMott et al. (2010; hereafter D10). The D10 equation (Eq. 1 below) was developed with measurements of activated INP concentrations derived using the continuous flow diffusion chamber (CFDC; Rogers et al., 2001). The INP measurements were made concurrently with measurements of the concentration of aerosol particles with diameter (D) larger than 0.5 µm ($n_{0.5}$)

$$N_{\mathrm{INP}}(T,\ n_{0.5}) = a \cdot (T_o - T)^b \cdot (n_{0.5})^{c\cdot(T_o-T)+d}. \quad (1)$$

Here T is the temperature in the section of the CFDC operated above water saturation, T_o is the reference temperature adopted by D10 (273.16 K, their Eq. 1), and a, b, c, and d are the fitted coefficients. We reexamine Eq. (1) because it was developed with the CFDC operating in a manner which restricted the upper-limit diameter of aerosol particles processed within the CFDC ($D < 1.6$ µm) and restricted the duration of the particle's exposure to water-saturated conditions ($t < 10$ s). Since both of these restrictions can cause INP concentrations to be underestimated (D10; Wright et al., 2013; DeMott et al., 2015), we use measurements made in and near clouds to evaluate the potential bias.

We have three specific objectives. First we use our airborne measurements of IC concentration to derive a temperature-dependent fit of those measurements. We refer to these two properties as N_{IC} and $N_{\mathrm{IC}}(T)$. Specifically, we analyze IC concentrations recorded within the downwind (descending flow) portion of middle-tropospheric wave clouds, where IC concentration is thought to reflect INP activation that occurred upwind, within the colder and liquid-water saturated portion of the cloud. Second, we use our measurements to derive a temperature- and aerosol-dependent fit of N_{IC} based on Eq. (1). We refer to the latter as $N_{\mathrm{IC}}(T, n_{0.5})$. Third, we analyze our measurement of N_{IC} with an estimate of the interval of time an air parcel was exposed to water saturation within a wave cloud. This is relevant to cloud modeling because many models employ a state- and time-dependent framework to predict IC concentration (e.g., Hoose et al., 2010). The INP, aerosol, and IC concentrations relevant to our work are summarized in Table 1.

The foundations of our investigation are the cold-season middle-tropospheric wave cloud studies of Cooper and Vali (1981), Cotton and Field (2002), Eidhammer et al. (2010), and Field et al. (2012). The prior research demonstrated that an assessment of wave cloud kinematics can be used to distinguish heterogeneous from homogeneous nucleation and that crystal production occurs primarily via the previously mentioned freezing nucleation pathways. Furthermore, no compelling evidence for secondary ice production was reported in those prior studies.

Our investigation is most similar to the airborne studies of Eidhammer et al. (2010) and Field et al. (2012). Those authors analyzed cold-season (late fall) measurements made near, and within, wave clouds during the ICE-L project conducted in 2007. Their measurements were made over northern Colorado and southern Wyoming. Our work is based on cold-season airborne measurements made during the Wyoming Airborne Integrated Cloud Observation (WAICO) study conducted 2008 and 2009 (Wang et al., 2012). We analyze measurements made at locations where a streamline model indicated our aircraft intersected air that ascended into, and descended from, wave clouds. As we will discuss in detail, we develop a data set from eight flights; 80 wave cloud streamlines are analyzed. In contrast, Eidhammer et al. (2010) analyzed data from one flight and modeled three streamlines. Field et al. (2012) expanded that analysis and reported on measurement/model comparisons for 28 streamlines. In their analyses, Eidhammer et al. (2010) and Field et al. (2012) exercised a streamline-following aerosol and cloud microphysical parcel model and derived the model's initial thermal state using measurements made downwind of the investigated wave clouds. In contrast, we use a streamline model to track the evolution of bulk thermodynamic properties (parcel microphysics is not evaluated), and we use thermodynamic measurements made immediately upwind of the investigated clouds, within ascending air, to initialize the model.

Table 1. Symbols used to represent aerosol, INP, and IC concentrations.

Symbol	Definition	Dimension
$n_{0.5}$	Measured aerosol concentration ($D > 0.5$ µm)	sccm^{-1} [a]
N_{IC}	Measured IC concentration ($D > 50$ µm)[b]	sL^{-1} [c]
$N_{\mathrm{IC}}(T)$	Temperature-dependent fit of IC concentration (see Sect. 4)	sL^{-1}
$N_{\mathrm{IC}}(T, n_{0.5})$	Temperature- and aerosol-dependent fit of IC concentration (see Sect. 4)	sL^{-1}
$N_{\mathrm{INP}}(T, n_{0.5})$	Temperature- and aerosol-dependent fit of INP concentration (D10) (see Eq. 1)	sL^{-1}

[a] Aerosol particle count per standard cubic centimeter at $P = 1.013 \times 10^5$ Pa and $T = 273.15$ K. [b] 2DC concentration for crystals sizing larger than 50 µm (see Sect. 2.2). [c] Particle count per standard liter at $P = 1.013 \times 10^5$ Pa and $T = 273.15$ K.

2 Measurements

All measurements were acquired onboard the University of Wyoming King Air (Wang et al., 2012). The base of operations was Laramie, Wyoming. All of the sampled clouds were in the altitude range 3700 to 7400 m and were located north of Laramie, within 110 km.

2.1 Temperature and humidity

Temperature (T) was measured using a reverse-flow immersion thermometer (Lawson and Cooper, 1990). Dew point temperature (T_{dp}) was derived from vapor density measurements made with a LI-COR gas analyzer (model LI6262). The latter is characterized by a 0.2 s time response (Dobosy et al., 1997) and this value is somewhat smaller than the time response of the reverse-flow temperature sensor (~ 1 s; Rodi and Spyers-Duran, 1972). The inlet to the LI-COR was forward facing and operated subisokinetically with its inlet airspeed set at approximately 18 m s^{-1}. The latter is a factor of 6 smaller than the airspeed of the King Air (110 m s^{-1}).

2.2 Microphysics

Three wing-mounted optical particle counters are used in this analysis: (1) the Passive Cavity Aerosol Spectrometer Probe (PCASP), (2) the Forward Scattering Spectrometer Probe (FSSP), and (3) the Two-Dimensional Optical Array Probe (2DC). Each of these was fabricated by Particle Measuring Systems (PMS; Boulder, CO).

The PCASP was used to measure the concentration of particles with diameters between 0.12 and 3.2 µm. Particle sizing was based on laboratory calibrations conducted using monodisperse test particles with refractive index $n = 1.59$ (Cai et al., 2013). PCASP concentrations were derived as the ratio of particle count rate divided by a calibrated sample flow rate (Cai et al., 2013).

Adiabatic compression warms the aerosol stream as it approaches the PCASP inlet. Strapp et al. (1992) estimated that this process occurs over 0.2 s. Once the stream reaches the probe, it is warmed by three anti-ice heaters (Particle Measuring Systems, 2002). The timescale for diabatic (anti-ice) heating is approximately 1 order of magnitude smaller than the adiabatic warming. Because of both the adiabatic and diabatic processes, unactivated cloud droplets (haze particles) and cloud droplets are partially evaporated prior to sizing within the PCASP. In the case of haze particles, evaporation is complete if the initial particle diameter is smaller than ~ 1 µm (Strapp et al., 1992; Snider and Petters, 2008).

The FSSP was used to categorize cloud droplets sizes from 1.5 to 47.5 µm into 15 bins. During WAICO the cloud droplet concentrations were less than 300 cm^{-3}, so the FSSP dead time and coincidence errors are less than 25 % (Baumgardner et al., 1985). Both of these effects were accounted for in the data processing. Because our FSSP measurements come from clouds containing ice, bias due to ice crystal shatter also needs to be addressed. Since we only analyze FSSP measurements recorded near the upwind edge of the clouds, where the ice crystals are small (< 100 µm) and their concentration is low (< 0.4 L^{-1}), the effect of shatter on the FSSP measurements is not expected to be significant (Gardiner and Hallett, 1985; Gayet et al., 1996; Field et al., 2003) and was not evaluated.

Ice crystals were sized and counted using an optical array probe (2DC) (Pokharel and Vali, 2011). This instrument records a crystal as a two-dimensional image. Some images were rejected using criteria described in Pokharel and Vali (2011). Images which passed the rejection tests were sized in the along-track direction (hereafter, this dimension is termed "diameter") and these were binned into channels with lower-limit diameters set at 25, 50, 100, 150, 200, 250, 300, and 400 µm for the smallest eight of 20 channels; nearly all crystals recorded during WAICO classified into these eight channels. Because even the largest crystals in this set are smaller than the size known to shatter when impacted at aircraft velocities (Korolev and Isaac, 2005; Korolev et al., 2013), the effect of shatter was ignored. Concentrations were derived by assuming that the optical depth of field, for all crystals and regardless of their size, was equal to the 2DC's sampling aperture (61 mm) (Vali et al., 1981). Crystal concentration and crystal interarrival time measurements, derived using the 2DC, are analyzed in greater detail in Appendix A.

2DC-derived concentrations were validated by Cooper and Saunders (1980). The basis for their validation was airborne 2DC concentrations measured simultaneous with concentrations derived by impacting ice crystals onto oil-coated slides (OCSs) exposed in a decelerator. Crystals impacted on the slides were photographed and counted, the counts were increased by dividing by a size-dependent impaction efficiency, and diameter-integrated concentrations were computed for crystals with maximum dimension larger than 50 µm. The OCS concentrations were compared to 2DC concentrations. The latter were derived by integrating from 50 µm to larger diameters. Cooper and Saunders reported 2DC-OCS concentration ratios between 3.6 and 0.6 ($\overline{x} = 1.7$, $\sigma = 0.9$, number of samples = 12). From the comparisons it was concluded that, for crystals larger than 50 µm, the 2DC is capable of making quantitative concentration measurements.

Based on the findings discussed in the previous paragraph we derived N_{IC} (Table 1) as the diameter-integrated concentration corresponding to $D > 50$ µm. We excluded from our analysis instances when the concentration of crystals in the first 2DC channel (25 to 50 µm) exceeded more than 50 % of the overall ($D > 25$ µm) diameter-integrated concentration. The intent of this criterion is avoidance of crystals whose concentration is uncertain because their depth of field is ambiguous. If we had summed those crystals into N_{IC}, the relative concentration bias could have approached a limiting value equal to the ratio of the 2DC manufacturer's recommendation for a 25 to 50 µm particle depth of field (~ 4 mm) divided by the sampling aperture (61 mm) (Strapp et al., 2001).

For both the PCASP and the 2DC, the relative Poisson sampling error was evaluated as the reciprocal of the square root of particle count.

2.3 Air motion

Vertical and horizontal air velocities were derived from differential pressure measurements made at the tip of the King Air's nose boom (Parish and Leon, 2013).

2.4 Lidar

The upward-pointing Wyoming Cloud Lidar (Wang et al., 2009, 2012) was used to remotely sense cloud boundaries. The lidar transmits in the near ultraviolet ($\lambda = 0.355\,\mu m$) at a pulse repetition frequency of 20 Hz. Seven lidar shots were averaged, making the time between samples 0.35 s. The vertical resolution of the lidar is 3.75 m. Using the lidar measurement of attenuated backscatter and depolarization, we evaluated the boundaries between clear air and liquid cloud and between liquid-dominated and ice-dominated cloud (Wang and Sassen, 2001).

In the next section we describe our determinations of the air parcel streamlines and how the lidar-derived cloud boundaries were used to evaluate the time interval, along the streamlines, within the liquid-dominated portions of the clouds.

3 Analysis

3.1 Parcel streamlines and parcel thermodynamic state

Here we explain how the streamlines were derived from measurements made during level-flight penetrations of 35 wave clouds. In our data set we have 19 penetrations made along the wind and 16 penetrations made against the wind. Also described is the parcel model we used to evaluate thermodynamic properties along the streamlines.

An average horizontal wind speed ($\bar{u}$) was derived from airborne in situ wind measurements made during each of the cloud penetrations. That average was applied as a constant in our streamline analysis. In contrast, the in situ measured vertical wind component (w) was oscillatory, so we fitted it as a sinusoid function versus along-track distance (x), and we assumed that the fitted vertical wind component ($w(x)$) did not vary vertically. Figure 1a shows the measured and fitted values of the vertical wind for a penetration that we showcase to illustrate our methods.

Within the ascending portion of the wave structure (e.g., to the left (upwind) of $x = 10.5$ km in Fig. 1a), we initialized several streamlines. The streamline center points were separated by ~ 550 m along the flight track (5 s at $110\,m\,s^{-1}$). For each of the center points the 1 Hz measurements of T, T_{dp}, and pressure (P) were used to derive five-second averaged values of T, T_{dp}, and P. These three properties were used to fix an air parcel's initial thermodynamic state. A closed parcel model, conserving potential temperature below the lifted condensation level (LCL), and equivalent potential temperature above the LCL was used to evaluate the thermodynamic state along a streamline. Using this model and the aforementioned descriptions of the horizontal and vertical wind components, we simulated the thermodynamic and kinematic evolution of streamline-following air parcels. One of the evaluated relationships is the parcel's temperature as a function of the along-track distance. An example of this is shown in Fig. 1d. Also indicated are the minimum streamline temperature (T_{low}) and the measurement of temperature (red circle) made at the downwind intersection of the flight track and the streamline.

We compared our streamline temperatures, each evaluated at the downwind track–streamline intersections, and the corresponding measured temperatures. The average absolute difference is 0.3 °C (number of samples = 80). This agreement is consistent with a small effect, smaller than the temperature measurement error (±0.5 °C), coming from violations of either the closed parcel assumption or the assumptions of vertically uniform $w(x)$ and constant $\bar{u}$.

3.2 Mixed-phase time

The interval of time during which an air parcel experiences water-saturated conditions was evaluated by combining the lidar measurements with the streamline information. We refer to this time interval as the mixed-phase time (t_{MP}). Figure 1b and c illustrate how t_{MP} was evaluated. At the upwind cloud edge, at $x = 9.5$ km but above the aircraft, the streamline encounters the first of two cloud boundaries. Using lidar measurements, we defined this upwind cloud boundary by its increased lidar backscatter and decreased lidar depolarization (compared to the depolarization in clear air). Approximately 4 km downwind, the streamline encounters the second boundary. We defined this boundary by its decreased lidar backscatter and increased depolarization. Here the boundary is between liquid- and ice-dominated cloud. Furthermore, we defined t_{MP} as the integral of the parcel transit time between these two boundaries. For a few of the streamlines, the downwind track–streamline intersection was within the liquid-cloud region. In those cases, the calculation of t_{MP} was stopped at the intersection. The lower and upper bounds of t_{MP} are 38 to 507 s; the average t_{MP} is 221 s.

We obtained good agreement between values of t_{MP}, based exclusively on lidar, and those based partially on the in situ measurements of T and T_{dp}. These comparisons were made by differencing the lidar-derived t_{MP} and a mixed-phase time derived using T- and T_{dp}-dependent determinations of the LCL (Sect. 3.1) combined with lidar-based determinations of the downwind cloud boundary. In this comparison the average absolute difference is 22 s. Each absolute difference was converted to a relative difference by dividing by the lidar-derived values of t_{MP}. The relative differences range from 0.0 to 0.9.

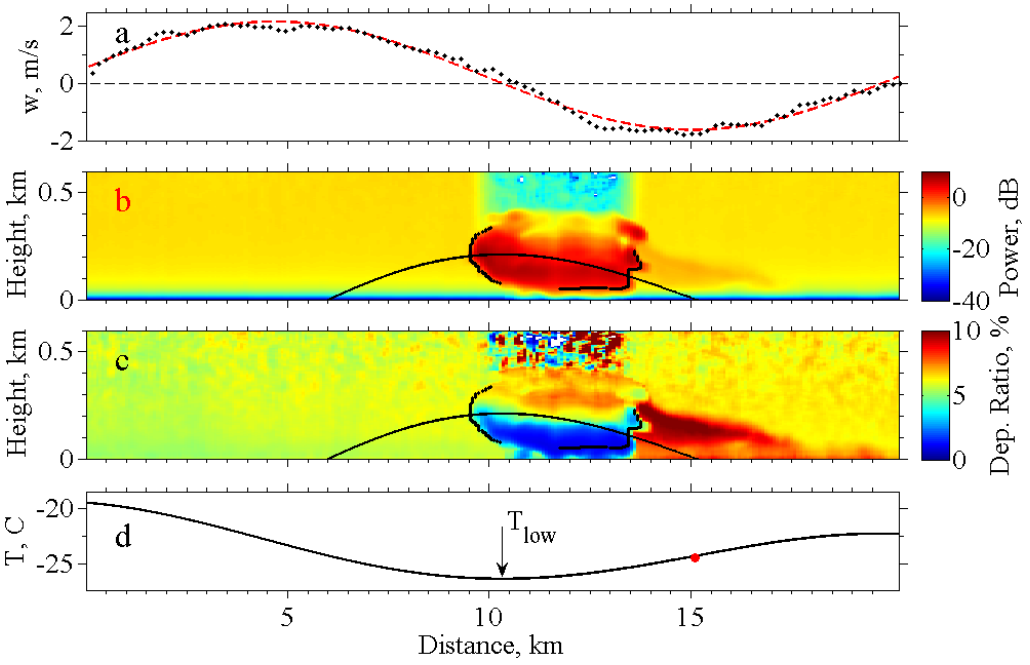

Figure 1. Level-flight sampling a few tens of meter below a wave cloud between 18:17:45 and 18:20:09 on 27 February 2008. Airflow is from left to right. **(a)** In situ vertical velocity measurements and the sinusoid fit. **(b)** The example streamline (black) overlain on lidar backscattered power; the two other black lines delineate the liquid-cloud and ice-cloud boundaries discussed in the text. **(c)** Example streamline overlain on lidar depolarization ratio; the two other black lines delineate the liquid-cloud and ice-cloud boundaries discussed in the text. **(d)** Streamline temperature, minimum streamline temperature, and the in situ measured temperature at the downwind track–streamline intersection (red circle).

3.3 Aerosol particles and cloud droplets

In this section we evaluate aerosol concentrations, measured outside of clouds, and compare to in-cloud droplet concentrations. For each of the 35 cloud penetrations we evaluated five-second averages of the PCASP and FSSP concentrations. For the PCASP, the averaging interval was started 5 s upwind of the cloud; for the FSSP, the averaging interval was started at the cloud edge. Averaging intervals are shown at the bottom of Fig. 2b and at the top of Fig. 2d. Also presented (Fig. 2a, b, and c) are the size-resolved concentrations from the PCASP, FSSP, and 2DC. The series shown in Fig. 2 are for the same section of flight illustrated in Fig. 1.

Similar to Eidhammer et al. (2010), we compared the upwind aerosol particle concentration ($D > 0.25\,\mu m$; five-second averaged) to the in-cloud droplet concentration ($D > 1.5\,\mu m$; five-second averaged). From the series presented in Fig. 2d, it can be seen that droplets, measured at $\sim x = 11\,km$ (i.e., downwind of the cloud edge), were more abundant than aerosol particles measured at $\sim x = 10.5\,km$ (i.e., upwind of the edge). Following this same averaging procedure, we evaluated a droplet-to-aerosol ratio for 32 of our 35 penetrations; three of the 35 were discarded because droplets were smaller than the minimum size detectable by the FSSP ($D = 1.5\,\mu m$). In the 32 comparisons, the droplet-to-aerosol concentration ratios were consistently greater than 0.7. These results are consistent with the findings of Eidhammer et al. (2010). A reasonable inference is that the $D > 0.25\,\mu m$ particles are internally mixed, the mixture's water-soluble fraction promoted the nucleation of the droplets, and the mixture's water-insoluble fraction promoted ice nucleation presumably via the condensation and immersion freezing pathways. The effect of ice development on cloud properties is evident at the downwind track–streamline intersection in Figs. 1 and 2. Most noticeable are the enhanced lidar depolarization ratios seen at $x \geq 15\,km$ in Fig. 1c and the enhanced diameter-integrated crystal concentrations seen at $x \geq 15\,km$ in Fig. 2d.

3.4 $D > 0.5\,\mu m$ aerosol particle and IC concentrations

In addition to the $D > 0.25\,\mu m$ aerosol concentrations analyzed in the previous section, we also evaluated $n_{0.5}$ (Sect. 1). These were averaged outside of the cloud during the five-second time windows used for thermodynamic-property averaging (Sect. 3.1). For the rest of the paper, $n_{0.5}$ is reported as a particle count per standard cubic centimeter ($sccm^{-1}$). Also for the rest of the paper, values of N_{IC} (Table 1) are derived as five-second averages evaluated at the downwind track–streamline intersections (e.g., at $\sim x = 15\,km$ in Fig. 1c), and these are reported as a crystal count per standard liter (sL^{-1}).

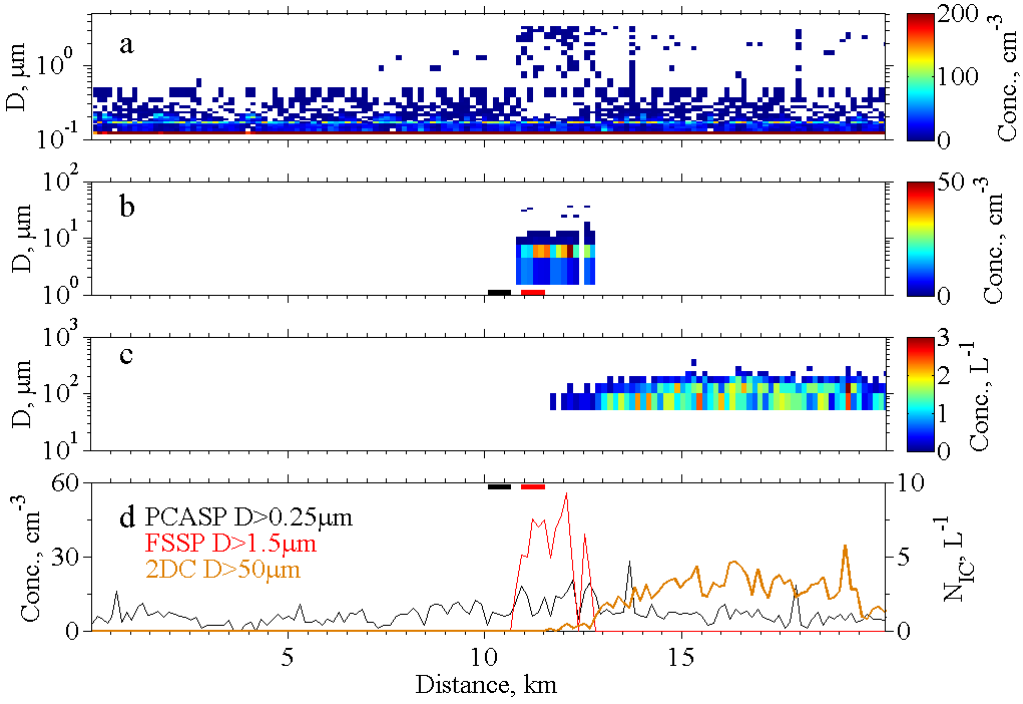

Figure 2. The same segment of flight as shown in Fig. 1. **(a)** Size-resolved PCASP concentrations. **(b)** Size-resolved FSSP concentrations. The black and red horizontal rectangles at the bottom of this panel are the five-second averaging intervals for aerosol and droplets analyzed in Sect. 3.3. **(c)** Size-resolved 2DC concentrations. **(d)** Diameter-integrated PCASP ($D > 0.25$ µm, black line), diameter-integrated FSSP ($D > 1.5$ µm, red line), and diameter-integrated 2DC ($D > 50$ µm, orange line) concentrations. Averaging intervals for aerosol and droplets are repeated from **(b)**.

3.5 Data set

In the previous sections we described how values of N_{IC}, $n_{0.5}$, T_{low}, and t_{MP} were evaluated for each streamline. The subset $\{N_{IC}, n_{0.5}, T_{low}\}$ is the streamline data we used to develop a fit of N_{IC}, according to the mathematical form of Eq. (1). However, before fitting our measurement data, we excluded streamlines affected by four effects: (1) an abundance of crystals in the first 2DC channel, (2) homogeneous freezing, (3) crystal sublimation, and (4) variable aerosol particle and crystal concentrations. Conditions for data *inclusion* are: (1) $N_{IC}(D < 50\,\mu m)$ must be smaller than $0.5 \times N_{IC}(D > 25\,\mu m)$ (Sect. 2.2); (2) $T_{low} > -35\,°C$ (Heymsfield and Miloshevich, 1993); (3) ice saturated, or larger relative humidity, at the downwind track–streamline intersection; and (4) relative Poisson sampling errors (Sect. 2.2) less than specified thresholds.[1] Out of the 116 streamlines we analyzed, 80 satisfy our data inclusion criteria. The set $\{N_{IC}, n_{0.5}, T_{low}, t_{MP}\}$ is provided for the 80 streamlines in the Supplement.

[1]The relative Poisson error thresholds adopted for IC concentration and for $n_{0.5}$ were 0.4 and 0.7, respectively. These values cut the distributions of the relative Poisson errors at their 99th percentiles.

4 Fitted N_{IC} equations

In this section we show results from fitting our measurement data with both temperature-dependent and temperature-aerosol-dependent equations. We start with a solely temperature-dependent fitting equation because many previous cloud modeling studies were based on such a relationship (e.g., Meyers et al., 1992) and because the rate of change of crystal concentration with temperature can have a profound impact on modeled cloud properties (Eidhammer et al., 2009).

We develop the fitting equations using logarithm-transformed crystal and logarithm-transformed aerosol concentrations. The reason for log transforming the data is that we expect errors, in both crystal and aerosol concentration, to be multiplicative in the sense that larger values correspond with larger error and vice versa. Multiplicative error, scaling in proportion to the square root of concentration as predicted by the Poisson probability law (Young, 1962; Rogers and Yau, 1989) was documented by Cai et al. (2013) in their investigations of the PCASP's response to steadily generated monodisperse test particles.

Figure 3a shows the temperature-dependent fit (i.e., $N_{IC}(T_{low})$) plotted versus measured N_{IC}. The square of the Pearson correlation coefficient (r^2), for this scatter plot, is

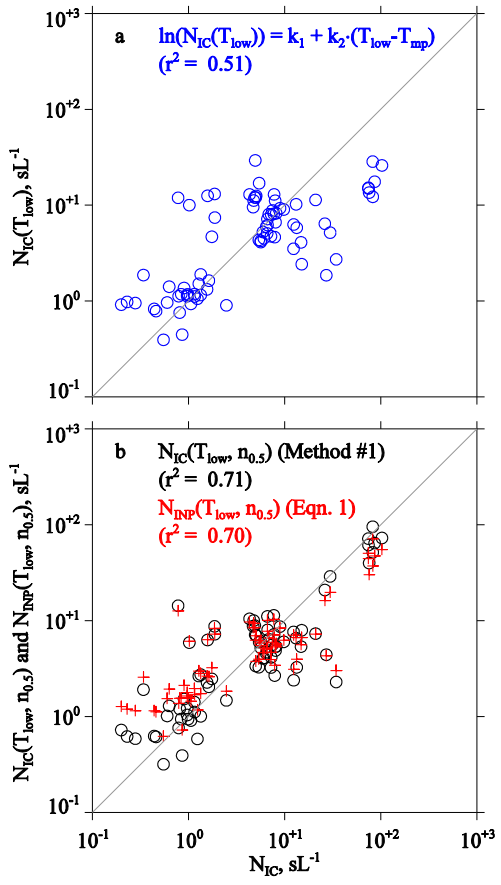

Figure 3. (a) Values of $N_{\mathrm{IC}}(T_{\mathrm{low}})$ $(\ln(N_{\mathrm{IC}}(T_{\mathrm{low}})) = k_1 + k_2 \cdot (T_{\mathrm{low}} - T_{\mathrm{MP}})$ with $T_{\mathrm{MP}} = 273.15\,\mathrm{K}$, $k_1 = -4.04$ and $k_2 = -0.22\,^{\circ}\mathrm{C}^{-1}$) plotted versus measured N_{IC}. **(b)** As in Fig. 3a but with $N_{\mathrm{IC}}(T_{\mathrm{low}}, n_{0.5})$ (method 1 fit coefficients) and $N_{\mathrm{INP}}(T_{\mathrm{low}}, n_{0.5})$ (Eq. 1 with D10's coefficients) plotted versus measured N_{IC}. In **(a)** and **(b)**, the square of the Pearson correlation coefficients (r^2) was evaluated using log-transformed concentrations. Also, the one-to-one line is shown in both panels.

relatively small and demonstrates that temperature alone, via the fit equation, can only explain 51 % of the N_{IC} variability.

In Fig. 3b we plot the temperature- and aerosol-dependent fit $N_{\mathrm{IC}}(T_{\mathrm{low}}, n_{0.5})$ versus measured N_{IC}. Results shown here are for one of two fitting methods we implemented. In fit method 1 we used the Matlab Curve Fitting Toolbox (The MathWorks, Natick, MA), with the log-transformed version of Eq. (1), and derived the logarithm of a ($\ln a$) and the values of b, c, and d. We also fitted the set $\{N_{\mathrm{IC}}, n_{0.5}, T_{\mathrm{low}}\}$ using the three-step procedure described in D10. We refer to the latter as method 2 and describe our implementation of that method in Appendix B. The advantage of method 1 is that it shortens D10's three-step procedure to one step.

The fit coefficients derived by D10, our fit coefficients (methods 1 and 2), and the statistical errors of methods 1 and 2 expressed as standard deviations are presented in Table 2. Focusing on results obtained using method 1, our four coefficients are seen to agree within 2 standard deviations of D10's. Also, agreement within 2 standard deviations was obtained between our application of method 2 and D10's.

By inputting the statistical errors from Table 2 into a propagation of error equation (Young, 1962; their Eq. 13.9), we evaluated contributions to the relative variance of the logarithm of $N_{\mathrm{IC}}(T_{\mathrm{low}}, n_{0.5})$ (method 1). For $n_{0.5} \leq 3.4\,\mathrm{sccm}^{-1}$ (the average for our data set) and for temperatures over the full range of our data set ($-34 \leq T_{\mathrm{low}} \leq -14\,^{\circ}\mathrm{C}$), the relative variance is controlled by terms proportional to both the square of the statistical error in $\ln a$ and the square of the statistical error in b. We also evaluated the fractional standard deviation of $N_{\mathrm{IC}}(T_{\mathrm{low}}, n_{0.5})$ (method 1). For the same $n_{0.5}$ and T_{low} settings provided above, the fractional standard deviation is ~ 4 and increases to ~ 5 if $n_{0.5}$ is set to $16\,\mathrm{sccm}^{-1}$ (the maximum for our data set). Yet, in spite of this uncertainty, our fitted (method 1) and measured values are seen to correlate over IC concentrations that range from 0.1 to $100\,\mathrm{sL}^{-1}$ (Fig. 3b). Also illustrated is a second set of fitted concentrations. These values of $N_{\mathrm{INP}}(T_{\mathrm{low}}, n_{0.5})$ were derived using Eq. (1) with D10's coefficients. For both sets of fitted concentrations (i.e., $N_{\mathrm{IC}}(T_{\mathrm{low}}, n_{0.5})$ and $N_{\mathrm{INP}}(T_{\mathrm{low}}, n_{0.5})$) the r^2 is ~ 0.7 and thus larger than that for the temperature-only fit (cf. Fig. 3a).

We also evaluated the fraction of the measured crystal concentrations that plot within a factor of 2 of the fit. Based on our method 1 coefficients, this percentage is 69 % and thus larger than the percentage (66 %) based on fit coefficients from D10 (the percentage is 71 % when using the method 2 coefficients; not shown here). Thus, we obtained better fitted-versus-measured agreement with our method 1 and method 2 fit coefficients and somewhat poorer agreement with the D10 coefficients.

5 Effect of mixed-phase time

As was discussed in the introduction, there is an outstanding question in atmospheric science community regarding the time-dependent nature of ice nucleation. Of relevance for our data set, with its average $t_{\mathrm{MP}} = 221\,\mathrm{s}$ (Sect. 3.2), is the possibility that the characteristic time for an embryo to transition to a crystal is comparable to t_{MP}. If that were the case, we would expect that streamlines associated with larger mixed-phase times, all other relevant properties the same, would have larger IC concentrations. The work of Vali and Snider (2015) provides an estimate of the effect. They show that time dependency can alter crystal concentrations by up to a factor of 3 depending on whether a time- and temperature-dependent parameterization, or a purely temperature-dependent parameterization, is used to describe heterogeneous ice nucleation.

We investigated time dependency by stratifying our 80 determinations of $\{N_{\mathrm{IC}}, n_{0.5}, T_{\mathrm{low}}, t_{\mathrm{MP}}\}$ into four T_{low} subsets. In Table 3 we present the subset's minimum and max-

Table 2. Equation (1) fit coefficients.

Coefficients	Fit D10[a]	Fit method 1	Statistical error method 1[b]	Fit method 2	Statistical error method 2[c]
$\ln a$	−9.73	−15.26	2.87	−15.03	4.11
b	3.33	4.94	0.88	4.86	1.30
c	0.0264	0.0028	0.0308	0.0038	0.034
d	0.0033	0.86	0.88	0.82	0.83

[a] Fit coefficients from D10. [b] The standard deviations for coefficients fitted via method 1. [c] The standard deviations for coefficients fitted via method 2.

Table 3. T_{low} subsets and the $\ln(N_{\mathrm{IC}})$ versus $\ln(t_{\mathrm{MP}})$ correlations

$T_{\min}$ °C	$T_{\max}$ °C	$\bar{n}_{0.5}$ sccm^{-1}	Number of samples	r[a]	p[b]
−34	−29	5.50	20	0.20	0.20
−29	−24	2.93	30	0.21	0.14
−24	−19	3.50	15	−0.05	0.57
−19	−14	2.57	15	0.06	0.44

[a] The Pearson correlation coefficient for the regression of $\ln(N_{\mathrm{IC}})$ versus $\ln(t_{\mathrm{MP}})$. [b] Level of significance, values of this parameter greater than $p = 0.05$ indicate an insignificant correlation.

imum temperatures, the averaged $n_{0.5}$, and the number of data values. For each of these we tested the hypothesis that $\ln(N_{\mathrm{IC}})$ is correlated with $\ln(t_{\mathrm{MP}})$. Values of the Pearson correlation coefficients (r) and the levels of significance (p) demonstrate that none of the correlations are significant (i.e., all have $p > 0.05$). This same conclusion was reached after removing from the correlations those points exhibiting the largest t_{MP} uncertainty (relative difference > 0.3, Sect. 3.2), but those results are not shown in Table 3. We also stratified by $n_{0.5}$ within the four T_{low} subsets. One of those correlations ($\ln(N_{\mathrm{IC}})$ versus $\ln(t_{\mathrm{MP}})$) approaches statistical significance, with $p = 0.1$ and with 10 paired values; the rest have $p > 0.1$. That subset plots in the gray rectangle shown in Fig. 4a and the N_{IC} versus t_{MP} correlation for that subset is shown in Fig. 4b.

In spite of these suggestions of a connection between crystal concentration and mixed-phase time we cannot argue convincingly that time-dependent effects were significant for crystals within the clouds we studied. Our ability to argue for, or against a dependence on t_{MP}, was limited by the strong temperature-dependence of ice nucleation. This is evident from Fig. 3a where the value $k_2 = -0.22\,^{\circ}\mathrm{C}^{-1}$ can be used to demonstrate that a 5 °C decrease corresponds to a factor of 3 increase in nucleated concentration. Also limiting are the relatively few data values within our four T_{low} subsets. Thus, in future wave cloud studies, attention should be paid to strategies which generate an adequate number of points within specified temperature and aerosol ranges.

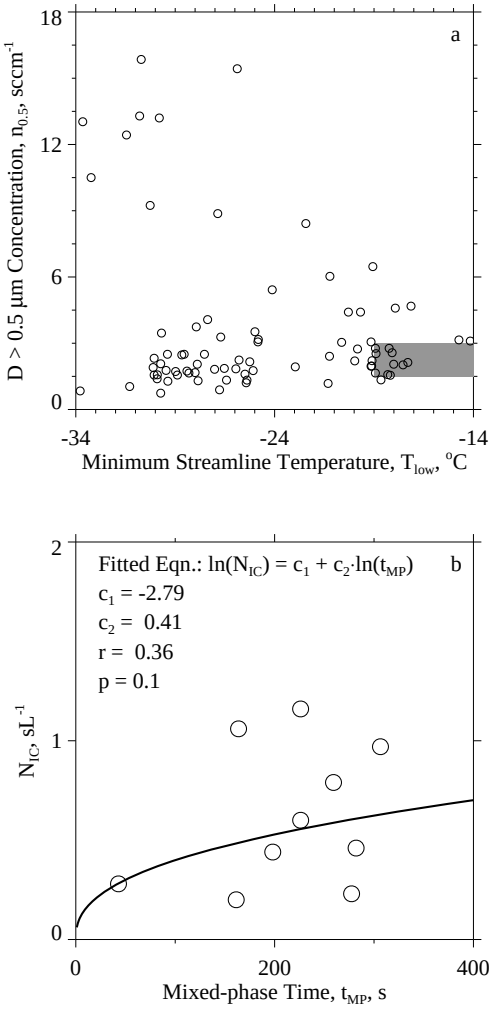

Figure 4. (a) The 80 paired values of $n_{0.5}$ and t_{MP} in our data set. The gray rectangle highlights the 10 points in the subset defined by $-19 \le T_{\mathrm{low}} < -14\,^{\circ}\mathrm{C}$ and $1.5 \le n_{0.5} < 3.0\,\mathrm{sccm}^{-1}$. **(b)** The 10 paired values of N_{IC} and t_{MP} from the gray rectangle shown in Fig. 4a. The black line is the fitting equation $\ln(N_{\mathrm{IC}}) = c_1 + c_2 \cdot \ln(t_{\mathrm{MP}})$. The Pearson correlation coefficient (r) and the level of significance (p) were evaluated using the log-transformed concentrations and log-transformed mixed-phase times.

6 Summary and conclusion

The result we present in Table 2, with fit coefficients generally consistent, in a statistical sense, with those reported by D10, is important because it validates D10's approach using different methodology. In short, we use a streamline model to connect a measurement of aerosol concentration ($n_{0.5}$), made upwind of a wave cloud, to a downwind measurement of IC concentration. Our reconfirmation of the relationship between crystals and $n_{0.5}$, implied by Eq. (1), is conceptually appealing because it acknowledges that aerosol particles are necessary for the occurrence of heterogeneous ice nucleation. Appeal also comes from the linkage provided by Eq. (1), through aerosol, to cloud processes.

We also probed the conjecture that the duration of INP exposure to water-saturated conditions is a determinant of IC concentration. Our analysis shows no statistically robust evidence for this. This finding is relevant to descriptions of ice nucleation within water-saturated layer clouds (e.g., stratocumulus and altostratus) where temperature is relatively uniform and steady and where time-dependent ice nucleation is suspected of occurring continuously and with substantial meteorological impact (Crosier et al., 2011; Westbrook and Illingworth, 2013). In fact, many model representations of heterogeneous nucleation anticipate this time-dependent, constant-temperature phenomenon. Also, in some models, the nucleation rate is set to 0 when the temperature tendency is 0 or positive (Khain et al., 2000; Muhlbauer and Lohmann, 2009), but this action is not supported by all of the experimental evidence currently available (for a review, see Vali, 2014). Further investigation is needed to confirm our conclusion of little, if any, time-dependent effect within the cloud type we studied (middle-tropospheric wave clouds). Going forward, we anticipate our methodology will help advance understanding of time-dependent atmospheric ice nucleation and atmospheric ice nucleation in general.

Appendix A

In this appendix we examine the reliability of ice crystal concentrations derived using the University of Wyoming 2DC. We derive concentrations using the Wyoming 2DC, with its slower-responding photodiode array (Gayet et al., 1993; Baumgardner and Korolev, 1997; Strapp et al., 2001), and compare to values derived using a faster-responding cloud imaging probe (CIP; Baumgardner et al., 2001). We also analyze the 2DC ice crystal interarrival times and investigate crystal shattering. Two data sets are analyzed. The first comes from Wyoming King Air flight data, acquired on 9 January 2011 during the Colorado Airborne Multi-Phase Cloud Study (CAMPS), and the second comes from the 80 downwind track–streamline intersections described in Sect. 3.5. Both the 2DC and CIP were operated with standard probe tips (Korolev et al., 2013).

Strapp et al. (2001) conducted laboratory studies that investigated a 2DC's ability to detect objects (circular dots) positioned away from the center of focus of the probe's laser. They demonstrated that the probe's finite response led to undersizing, counting losses, and image distortion. In the case of dot sizes smaller than 100 µm, undersizing and counting losses increased with the speed the dots transited through the probe's sample volume. Strapp et al. conducted their testing using dots deposited onto a glass disk. The dots were opaque, monodisperse, and regularly spaced on the disk along circular tracks. The disk was positioned with its rotational axis parallel to the 2DC laser beam. The position of the disk plane, relative to the center of focus of the beam, was varied. The largest dot speeds tested by Strapp et al. were comparable to the airspeed of the Wyoming King Air ($\sim 100\,\mathrm{m\,s^{-1}}$).

A1 2DC and CIP concentrations

A comparison of 2DC- and CIP-derived concentrations was made using Wyoming King Air data acquired on 9 January 2011. The comparison data were selected from three level-flight transits of an orographic cloud. The cloud was located over continental divide in northern Colorado. During the cloud transits the liquid water content was less than $0.2\,\mathrm{g\,m^{-3}}$ and temperature was between -23 and $-25\,^{\circ}\mathrm{C}$. We processed the raw 2DC and CIP measurements the same way we processed the WAICO 2DC measurements (Sect. 2.2). Also consistent with the WAICO processing, the compared concentrations are five-second averages and are for crystals larger than 50 µm (sized along the aircraft track). The CIP/2DC comparison is shown in Fig. A1a. The vertical line at $5\,\mathrm{L^{-1}}$ marks the median of the 80 concentrations in our WAICO data set (Sect. 3.5), and its implication is discussed in the following paragraph.

Because of the undersizing and counting losses documented for a 2DC, especially at the low end of its range ($D < 100$ µm), and the fact these effects are attributed to the relatively slow time response of the 2DC's optical array

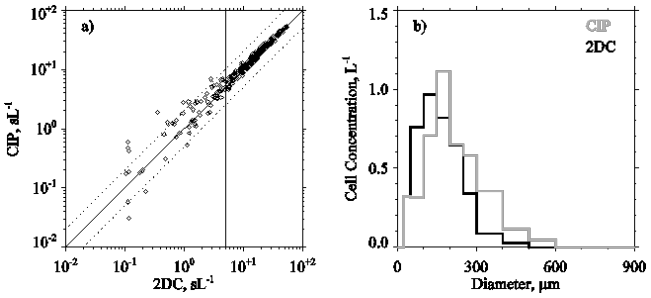

Figure A1. (a) The CIP/2DC concentration comparison. Compared values are five-second averages and are for crystals larger than 50 µm. Comparison data is from 9 January 2011 during the Colorado Airborne Multi-Phase Cloud Study (CAMPS). Wyoming King Air data shown here was selected from three along-wind level-flight cloud transits: (1) 22:12:00 to 22:22:00 UTC, (2) 22:39:00 to 22:48:00 UTC, and (3) 23:06:00 to 23:16:00 UTC. The vertical line at $5\,\mathrm{sL^{-1}}$ is drawn at the median value for our set of 80 WAICO 2DC-derived measurements. **(b)** 2DC and CIP size distributions from a representative five-second subset (22:46:46 to 22:46:50 UTC) of the flight on 9 January 2011.

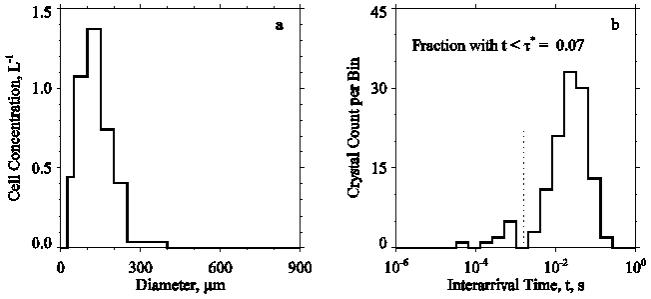

Figure A2. (a) The 2DC size distribution derived for the WAICO 18:19:33 to 18:19:37 UTC interval on 27 February 2008. This interval corresponds to the downwind track–streamline intersection at $x = 15$ km in Fig. 1c. **(b)** The interarrival time histogram for the 18:19:33 to 18:19:37 UTC interval on 27 February 2008. The vertical dashed line marks a minimum between a fragment mode ($t < \tau^*$) and a mode corresponding to intact crystals ($t > \tau^*$).

(Strapp et al., 2001), we expected that concentrations derived using the faster-responding CIP (Baumgardner et al., 2001) would exceed 2DC-derived values. Contrary to that expectation, we found reasonable agreement (Fig. A1a). Measures of the agreement are as follows: (1) for concentrations larger than $5\,\mathrm{sL^{-1}}$, all of the 2DC-derived values plot well within a factor of 2 of the CIP. (2) For concentrations smaller than $5\,\mathrm{sL^{-1}}$, a large fraction of the 2DC values (87 %) plot within a factor of 2 of the CIP. These findings, combined with the findings of Cooper and Saunders (1980) (also see Sect. 2.2), lend confidence to the concentration values we derived using 2DC measurements made during WAICO. However, this comparison does not completely lessen the concern that we biased the WAICO concentrations at $D < 100$ µm by assuming that the 2DC's optical depth of field was independent

of crystal size and equal to the probe's sampling aperture (61 mm) (Vali et al., 1981 and Sect. 2.2).

A2 Interarrival time and shattering

Representative CIP and 2DC size distributions, from CAMPS, are shown in Fig. A1b. It is evident that most of the detected crystals are smaller than 400 µm, especially in the 2DC measurement. A size distribution from one of the 80 WAICO downwind track–streamline intersections is shown in Fig. A2a. The largest crystal detected in this five-second interval is 400 µm. The figure also demonstrates that the diameter-integrated concentrations $N_{\mathrm{IC}}(D > 100\,\mu\mathrm{m})$ and $N_{\mathrm{IC}}(D > 50\,\mu\mathrm{m})$ are comparable and that the ratio $N_{\mathrm{IC}}(D > 100\,\mu\mathrm{m}) / N_{\mathrm{IC}}(D > 50\,\mu\mathrm{m})$ is only somewhat smaller than unity; for our 80 size distributions the average ratio is 0.7.

A histogram of crystal interarrival times from WAICO is shown in Fig. A2b. Evident in the left tail of the histogram is a minimum, at interarrival time $\tau^* = 2 \times 10^{-3}$ s, where we delineate between a fragment mode ($t < \tau^*$) and a mode corresponding to intact crystals ($t > \tau^*$). We note that only 7 % of the crystal counts classify as fragments and that this fraction is much smaller than the example presented by Korolev et al. (2013) for a 2DC with standard probe tips (their Fig. 14a).

We analyzed interarrival times obtained from each of the 80 WAICO downwind track–streamline intersections. Histograms were binned as in Fig. A2b (3.5 bins per decade) and all particle images, including those that did not pass the rejection criteria of Pokharel and Vali (2011) (Sect. 2.2), were used. We developed a procedure that searches the histogram for a minimum between $t = 10^{-6}$ s and the histogram mode. In our set of 80 there are 16 cases that do not exhibit a minimum and 21 with a provisionally significant minimum. The provisional cases were characterized by a cumulative fraction, evaluated at the minimum, greater than 20 %. The example shown in Fig. A2b is not a provisional case because the cumulative fraction at $\tau^* = 2 \times 10^{-3}$ s is less than 20 %. All of the provisional cases exhibited a minimum that was within 1 order of magnitude of the histogram mode. Because order-of-magnitude separation is substantially less than the minimum-to-mode separation seen Korolev et al. (2013) (their Fig. 14), we concluded that a fragment mode could not be discerned. Thus, we ignored the effect of shattering. Of the remaining 43 cases ($43 = 80 - 16 - 21$), 26 had a minimum more than 1 order of magnitude smaller than the histogram mode; Fig. A2b is an example. For these we ignored the effect of shattering because the fraction affected was less than 20 % and because the rejection criteria of Pokharel and Vali (2011) remove some of the affected crystals from the population used to evaluate the concentration.

Appendix B

Here we describe how we fitted our 80 determinations of the set $\{N_{\mathrm{IC}},\ n_{0.5},\ T_{\mathrm{low}}\}$ using the three-step procedure developed by D10 (herein method 2). In the first step, the data were binned into four T_{low} subsets; the number of samples in the four subsets is provided in Table 3. In the second step, values of $\ln(p_i)$ and q_i were derived for each subset by regression. Here "i" indicates the temperature subset and the form of the regression equation is

$$\ln\left(N_{\mathrm{IC},i}\right) = \ln(p_i) + q_i \cdot \ln\left(n_{0.5,i}\right). \tag{B1}$$

In the third step, the values of $\ln(p_i)$ were regressed versus $\ln\left(T_o - T_{\mathrm{low};i}\right)$ and the values of q_i were also regressed versus $\left(T_o - T_{\mathrm{low};i}\right)$. In these regressions $T_{\mathrm{low},i}$ is the average of the subset. The slopes and intercepts of these regressions define the method 2 coefficients $\ln a$, b, c, and d:

$$\ln a = \text{intercept}(\ln(p_i) \text{ versus } \ln(T_o - T_{\mathrm{low};i})) \tag{B2}$$

$$b = \text{slope}(\ln(p_i) \text{ versus } \ln(T_o - T_{\mathrm{low};i})) \tag{B3}$$

$$c = \text{slope}(q_i \text{ versus } (T_o - T_{\mathrm{low};i})) \tag{B4}$$

$$d = \text{intercept}(q_i \text{ versus } (T_o - T_{\mathrm{low};i})). \tag{B5}$$

The Supplement related to this article is available online at doi:10.5194/acp-15-6113-2015-supplement.

Acknowledgements. Data collection and initial analyses were supported by NSF under Award AGS-0645644. The authors thank Alfred Rodi, Jeffrey French, Larry Oolman, Matthew Burkhart and Perry Wechsler for the assistance they provided during the field and analysis phases of the project. The authors also thank Paul DeMott, who critiqued an early draft of the paper. Critiques provided by the reviewers are appreciated. J. R. Snider acknowledges support from NSF grant AGS1034858.

Edited by: M. Krämer

References

Baumgardner, D. and Korolev, A.: Airspeed corrections for optical array probe sample volumes, J. Atmos. Ocean. Technol., 14, 1224–1229, 1997.

Baumgardner, D., Strapp, W., and Dye, J. E.: Evaluation of the forward scattering spectrometer probe. Part II: Corrections for coincidence and dead-time losses, J. Atmos. Oceanic Tech., 2, 626–632, 1985.

Baumgardner, D., Jonsson, H., Dawson, W., O'Connor, D., and Newton, R.: The cloud, aerosol and precipitation spectrometer: a new instrument for cloud investigations, Atmos. Res., 59–60, 251–264, 2001.

Bigg, E. K.: The supercooling of water, Proc. Phys. Soc. B., 66, 688–694, 1953.

Braham, R. R. and Squires, P.: Cloud Physics-1974, Bull. Amer. Meteor. Soc., 55, 543–586, 1974.

Cai, Y., Snider, J. R., and Wechsler, P.: Calibration of the passive cavity aerosol spectrometer probe for airborne determination of the size distribution, Atmos. Meas. Tech., 6, 2349–2358, doi:10.5194/amt-6-2349-2013, 2013.

Cantrell, W. and Heymsfield, A.: Production of ice in tropospheric clouds: A review, Bull. Amer. Meteor. Soc., 86, 795–807, 2005.

Cooper, W. A. and Saunders, C. P. R.: Winter storms over the San Juan Mountains. Part II: Microphysical processes, J. Appl. Meteor., 19, 927–941, 1980.

Cooper, W. A. and Vali, G.: The origin of ice in mountain cap clouds, J. Atmos. Sci., 38, 1244–1259, 1981.

Cotton, R. and Field, P.: Ice nucleation characteristics of an isolated wave cloud, Q. J. Roy. Meteor. Soc., 128, 2417–2437, 2002.

Crosier, J., Bower, K. N., Choularton, T. W., Westbrook, C. D., Connolly, P. J., Cui, Z. Q., Crawford, I. P., Capes, G. L., Coe, H., Dorsey, J. R., Williams, P. I., Illingworth, A. J., Gallagher, M. W., and Blyth, A. M.: Observations of ice multiplication in a weakly convective cell embedded in supercooled mid-level stratus, Atmos. Chem. Phys., 11, 257–273, doi:10.5194/acp-11-257-2011, 2011.

DeMott, P. J., Prenni, A. J., Liu, X., Kreidenweis, S. M., Petters, M. D., Twohy, C. H., Richardson, M. S., Eidhammer, T., and Rogers, D. C.: Predicting global atmospheric ice nuclei distributions and their impacts on climate, P. Natl. Acad. Sci., 107, 11217–11222, 2010.

DeMott, P. J., Prenni, A. J., McMeeking, G. R., Sullivan, R. C., Petters, M. D., Tobo, Y., Niemand, M., Möhler, O., Snider, J. R., Wang, Z., and Kreidenweis, S. M.: Integrating laboratory and field data to quantify the immersion freezing ice nucleation activity of mineral dust particles, Atmos. Chem. Phys., 15, 393–409, doi:10.5194/acp-15-393-2015, 2015.

Dobosy, R. J., Crawford, T. L., MacPherson, J. I., Desjardins, R. L., Kelly, R. D., Oncley, S. P., and Lenschow, D. H.: Intercomparison among four flux aircraft at BOREAS in 1994, J. Geophys. Res.-Atmos., 102, 29101–29111, 1997.

Eidhammer, T., DeMott, P. J., and Kreidenweis, S. M.: A comparison of heterogeneous ice nucleation parameterizations using a parcel model framework, J. Geophys. Res., 114, D06202, doi:10.1029/2008JD011095, 2009.

Eidhammer, T., DeMott, P. J., Prenni, A. J., Petters, M. D., Twohy, C. H., Rogers, D. C., Stith, J., Heymsfield, A., Wang, Z., Pratt, K. A., Prather, K. A., Murphy, S. M., Seinfeld, J. H., Subramanian, R., and Kreidenweis, S. M.: Ice initiation by aerosol particles: Measured and predicted ice nuclei concentrations versus measured ice crystal concentrations in an orographic wave cloud, J. Atmos. Sci., 67, 2417–2436, 2010.

Field, P. R., Wood, R., Brown, P. R. A., Kaye, P. H., Hirst, E., Greenaway, R., and Smith, J. A.: Ice particle interarrival times measured with a fast FSSP, J. Atmos. Oceanic Tech., 20, 249–261, 2003.

Field, P. R., Heymsfield, A. J., Shipway, B. J., DeMott, P. J., Pratt, K. A., Rogers, D. C., Stith, J., and Prather, J. K. A.: Ice in clouds experiment-layer clouds. Part II: Testing characteristics of heterogeneous ice formation in lee wave clouds, J. Atmos. Sci., 69, 1066–1079, 2012.

Gardiner, B. A. and Hallett, J.: Degradation of in-cloud forward scattering spectrometer probe measurements in the presence of ice particles, J. Atmos. Ocean. Technol., 2, 171–180, 1985.

Gayet, J. F., Brown, P. R. A., and Albers, F.: A Comparison of In-Cloud Measurements Obtained with Six PMS 2D-C Probesm J. Atmos. Ocean. Technol., 10, 180–194, 1993.

Gayet, J. F., Febvre, G., and Larsen, H.: The reliability of the PMS FSSP in the presence of small tee crystals, J. Atmos. Ocean. Technol., 13, 1300–1310, 1996.

Hoose, C., Kristjánsson, J. E., Chen, J.-P., and Hazra, A.: A classical-theory-based parameterization of heterogeneous ice nucleation by mineral dust, soot and biological particles in a global climate model, J. Atmos. Sci., 67, 2483–2503, 2010.

Heymsfield, A. J. and Miloshevich, L. M.: Homogeneous ice nucleation and supercooled liquid water in orographic wave clouds, J. Atmos. Sci., 50, 2335–2353, 1993.

Khain, A. P., Ovtchinnikov, M., Pinsky, M., Pokrovsky, A., and Krugliak, H.: Notes on the state-of-the-art numerical modeling of cloud microphysics, Atmos. Res., 55, 159–224, 2000.

Korolev, A. V. and Isaac, G. A.: Shattering during sampling by OAPs and HVPS. Part I: Snow particles, J. Atmos. Ocean. Technol., 22, 528–542, 2005.

Korolev, A. V., Emery, E. F., Strapp, J. W., Cober, S. G., and Isaac, G. A.: Quantification of the effects of shattering on airborne ice particle measurements, J. Atmos. Ocean. Technol., 30, 2527–2553, 2013.

Lawson, R. P. and Cooper, W. A.: Performance of some airborne thermometers in clouds, J. Atmos. Ocean. Technol., 7, 480–494, 1990.

Meyers, M. P., DeMott, P. J., and Cotton, W. R.: New primary ice-nucleation parameterizations in an explicit cloud model, J. Appl. Meteor., 31, 708–721, 1992.

Muhlbauer, A. and Lohmann, U.: Sensitivity studies of aerosol–cloud interactions in mixed-phase orographic precipitation, J. Atmos. Sci., 66, 2517–2538, doi:10.1175/2009JAS3001.1, 2009.

Murray, B. J., O'Sullivan, D., Atkinson, J. D., and Webb, M. E.: Ice nucleation by particles immersed in supercooled cloud droplets, Chem. Soc. Rev., 41, 6519–6554, 2012.

Niemand, M., Möhler, O., Vogel, B., Vogel, H., Hoose, C., Connolly, P., Klein, H., Bingemer, H., DeMott, P., Skrotzki, J., and Leisner, T.: A particle-surface-area-based parameterization of immersion freezing on desert dust particles, J. Atmos. Sci., 69, 3077–3092, 2012.

Parish, T. R. and Leon, D.: Measurement of Cloud Perturbation Pressures Using an Instrumented Aircraft, J. Atmos. Ocean. Technol., 30, 215–229, 2013.

Particle Measuring Systems: Passive Cavity Aerosol Spectrometer Probe (Airborne), PMS Model PCASP-100X 0.10 – 3.0 μm Operating Manual, PMS Inc., Boulder, CO, 2002.

Pokharel, B. and Vali, G.: Evaluation of collocated measurements of radar reflectivity and particle sizes in ice clouds, J. Appl. Meteorol., 50, 2104–2119, 2011.

Rodi, A. R. and Spyers-Duran, P. A.: Analysis of time response of airborne temperature sensors, J. Appl. Meteorol., 11, 554–556, 1972.

Rogers, R. R. and Yau, M. K.: A Short Course in Cloud Physics, 3rd Edn. Permagon Press, 304 pp., 1989.

Rogers, D. C., DeMott, P. J., Kreidenweis, S. M., and Chen, Y. L.: A continuous-flow diffusion chamber for airborne measurements of ice nuclei, J. Atmos. Ocean. Technol., 18, 725–741, 2001.

Snider, J. R. and Petters, M. D.: Optical particle counter measurement of marine aerosol hygroscopic growth, Atmos. Chem. Phys., 8, 1949–1962, doi:10.5194/acp-8-1949-2008, 2008.

Strapp, J. W., Leaitch, W. R., and Liu, P. S. K.: Hydrated and dried aerosol-size-distribution measurements from the particle measuring systems FSSP-300 probe and the deiced PCASP-100x Probe, J. Atmos. Ocean. Technol., 9, 548–555, 1992.

Strapp, J. W., Albers, F., Reuter, A., Korolev, A. V., Maixner, U., Rashke, E., and Vukovic, Z.: Laboratory measurements of the response of a PMS OAP-2DC, J. Atmos. Ocean. Technol., 18, 1150–1170, 2001.

Wang, Z. and Sassen, K.: Cloud type and macrophysical property retrieval using multiple remote sensors, J. Appl. Meteor., 40, 1665–1682, 2001.

Wang, Z., Wechsler, P., Kuestner, W., French, J., Rodi, A., Glover, B., Burkhart, M., and Lukens, D.: Wyoming Cloud Lidar: instrument description and applications, Opt. Express, 17, 13576–13587, 2009.

Wang, Z., French, J., Vali, G., Wechsler, P., Haimov, S., Rodi, A., Deng, M., Leon, D., Snider, J., and Peng, L.: Single aircraft integration of remote sensing and in situ sampling for the study of cloud microphysics and dynamics, Bull. Am. Meteorol. Soc., 93, 653–668, 2012.

Westbrook, C. D. and Illingworth, A. J.: The formation of ice in a long-lived supercooled layer cloud, Q. J. Roy. Meteor. Soc., 139, 2209–2221, 2013.

Wright, T. P., Petters, M. D., Hader, J. D., Morton, T., and Holder, A. L.: Minimal cooling rate dependence of ice nuclei activity in the immersion mode, J. Geophys. Res. Atmos., 118, 10535–10543, doi:10.1002/jgrd.50810, 2013.

Vali, G.: Nucleation terminology, Bull. Am. Meteorol. Soc., 66, 1426–1427, 1985.

Vali, G.: Interpretation of freezing nucleation experiments: singular and stochastic; sites and surfaces, Atmos. Chem. Phys., 14, 5271–5294, doi:10.5194/acp-14-5271-2014, 2014.

Vali, G. and Snider, J. R.: Time-dependent freezing rate parcel model, Atmos. Chem. Phys., 15, 2071–2079, doi:10.5194/acp-15-2071-2015, 2015.

Vali, G. and Stansbury, E. J.: Time-dependent characteristics of the heterogeneous nucleation of ice, Can. J. Phys., 44, 477–502, 1966.

Vali, G., Politovich, M. K., and Baumgardner, D. G.: Conduct of cloud spectra measurements, Report AFGL-TR-81-0122, Air Force Geoph. Lab., available from Nat'l. Techn. Inf. Serv., Order No. AD-A102944/6, 1981.

Young, H. D.: Statistical Treatment of Experimental Data, McGraw-Hill Book Company, 107 pp., 1962.